ACS OMEGA

http://pubs.acs.org/journal/acsodf

Article

Simple Low Temperature Technique to Synthesize Sillenite Bismuth Ferrite with Promising Photocatalytic Performance

Fahmida Sharmin and M. A. Basith*

Cite This: *ACS Omega* 2022, 7, 34901−34911

Read Online

ACCESS | Metrics & More | Article Recommendations | Supporting Information

ABSTRACT: Sillenite-type members of the bismuth ferrite family have demonstrated outstanding potential as novel photocatalysts in environmental remediation such as organic pollutant degradation. This investigation has developed a low temperature one-step hydrothermal technique to fabricate sillenite bismuth ferrite $Bi_{25}FeO_{40}$ (S-BFO) via co-substitution of 10% Gd and 10% Cr in Bi and Fe sites of $BiFeO_3$, respectively, by tuning hydrothermal reaction temperatures. Rietveld refined X-ray diffraction patterns of the as-synthesized powder materials revealed the formation of S-BFO at a reaction temperature of 120−160 °C. A further increase in the reaction temperature destroyed the desired sillenite structure. With the increase in the reaction temperature from 120 to 160 °C, the morphology of S-BFO gradually changed from irregular shape to spherical powder nanomaterials. The high-resolution TEM imaging demonstrated the polycrystalline nature of the S-BFO(160) nanopowders synthesized at 160 °C. The as-synthesized samples exhibited considerably high absorbance in the visible region of the solar spectrum, with the lowest band gap of 1.76 eV for the sample S-BFO(160). Interestingly, S-BFO(160) exhibited the highest photocatalytic performance under solar irradiation, toward the degradation of rhodamine B and methylene blue dyes owing to homogeneous phase distribution, regular powder-like morphology, lowest band gap, and quenching of electron−hole pair recombination. The photodegradation of a colorless organic pollutant (ciprofloxacin) was also examined to ensure that the degradation is photocatalytic and not dye-sensitized. In summary, Gd and Cr co-doping have proven to be a compelling energy-saving and low-cost approach for the formulation of sillenite-phase bismuth ferrite with promising photocatalytic activity.

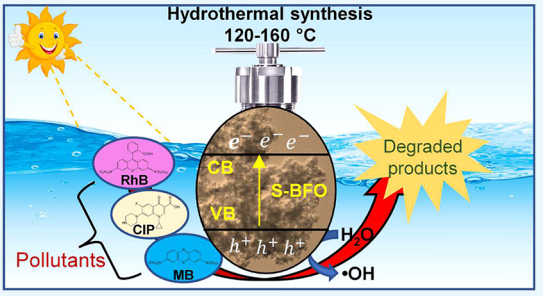

INTRODUCTION

In the last few decades, semiconductor photocatalysis has been regarded as a promising technology for deteriorating toxic organic pollutants such as dyes and antibiotics from wastewater.[1,2] Environmental remediation with photocatalysts has two advantages: first, it converts pollutants from complex molecules to simpler, non-toxic ones, and second, it avoids the need for additional treatment, disposal, or usage of high-cost oxidizing chemicals by employing solar energy.[3] The majority of research has so far focused on the titania (TiO_2) photocatalyst, which has a strong oxidizing ability and chemical stability.[4] However, due to its wide band gap (E_g = 3.2 eV), titania only responds to ultraviolet irradiation, which accounts for only ∼3−4% of the whole solar spectrum.[5] Hence, developing new visible light-active photocatalysts is of significant research and technological interest among the scientific community.[6−8]

Bismuth ferrites, a large group of transition-metal oxides, including perovskite, mullite, and sillenite-type structural compounds have lately sparked the interest of researchers due to their superior fundamental physics and wide-ranging technological applications.[9,10] Among them, perovskite-type $BiFeO_3$ (BFO) with a suitable band gap of ∼2.2 eV and the existence of simultaneous ferroelectric and ferromagnetic ordering at room temperature is mostly studied in the field of visible-light responsive photocatalysis.[11] Compared to perovskite BFO, the synthesis and analysis of other phases such as sillenite-type $Bi_{25}FeO_{40}$ with the *I*23 cubic crystal structure are yet less explored.[12,13] The sillenite compounds, bearing the general formula of $Bi_{12}MO_{20}$ (M = Ge, Ti, Ga, Fe, Bi, V, etc), exhibit unique properties such as photo-refractivity, optical activity, and photo-conductivity.[14] So far, investigations on sillenites such as $Bi_{12}TiO_{20}$,[15] $Bi_{24}Ga_2O_{39}$,[16] and $Bi_{24}AlO_{39}$[17] have demonstrated promising photocatalytic activity due to the presence of Bi−O polyhedra within the $Bi_{12}MO_{20}$ crystal structure. It has been reported that such a polyhedron arrangement of Bi−O may result in a dipole moment of 0.174 Debye and might suppress the electron−hole pair recombination, thereby significantly facilitating the activity of the photocatalysts.[18]

Received: June 2, 2022
Accepted: September 9, 2022
Published: September 23, 2022

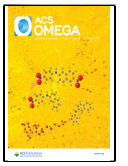

The sillenite-type $Bi_{25}FeO_{40}$ was also found to exhibit promising photocatalytic performance to degrade various toxic compounds from wastewater. It has been revealed in the previous investigation[19] that using the hydrothermal technique, the formation of sillenite-phase and perovskite-phase BFO mainly depends on the reaction time and temperatures. However, stabilization of the sillenite crystal structure is quite challenging due to its metastable nature. For instance, Verma et al.[20] have reported the formation of rhombohedral structured BFO with the *R*3*c* space group, following the sol–gel auto-combustion technique where the presence of sillenite and mullite phases was unavoidable. Zhou et al.[21] have demonstrated that following the facile hydrothermal technique, the sillenite-phase $Bi_{25}FeO_{40}$ was formed at the initial stage of the synthesis, and as the reaction time extended, the sillenite phase was gradually transformed into the rhombohedral phase. In a previous investigation,[22] we have also reported the same phenomenon where the increase in the hydrothermal reaction temperature has resulted in the sillenite to rhombohedral phase transition. However, in some previous investigations,[23,24] the substitution of dopants in the Bi and/or Fe site of BFO has succeeded in changing the microstructure of the parent by introducing distortions in the lattice structure and thereby triggering phase transitions. For instance, in a previous investigation,[23] doping with 10% Gd and 20% Co resulted in the phase transition from rhombohedral to sillenite phase, following a sol–gel method. In another investigation,[24] the stabilization of sillenite-phase $Bi_{25}FeO_{40}$ was observed, with 10% Ni^{2+} substitution in the Fe site of $BiFeO_3$, following the high energy ball milling method. In that investigation, the formation of sillenite was ascribed to the reduction of Fe^{3+} to Fe^{2+} due to the substitution of Fe^{3+} by Ni^{2+}.

Notably, $Bi_{25}FeO_{40}$, with a smaller band gap of ∼1.8 eV, is thought to be a potential visible-light response material, and its superparamagnetic nature may also provide an extra advantage for easy separation and recovery of the photocatalyst from the reaction medium.[25] However, compared to perovskite BFO, there has been seldom comprehensive investigation on, especially, the photocatalytic performance of the sillenite $Bi_{25}FeO_{40}$. In most of the earlier investigations[26,27] on the $Bi_{25}FeO_{40}$ photocatalyst, the synthesis was conducted at comparatively high reaction temperatures with long time-consuming steps, which resulted in large grain-sized final products. It is to be noted that in a few prior low temperature hydrothermal fabrications,[21,28] either the obtained sillenite BFO phases were not scrutinized by Rietveld or relevant analyses or the experiments were performed at a certain temperature with prolonged reaction time (about 20–24 h). Interestingly, in the present investigation, we have synthesized sillenite-phase bismuth ferrite with nanopowder-like morphology at a lower reaction temperature of 120–160 °C, following a simple, energy-saving, and cost-effective hydrothermal technique within only 6 h of reaction time without any pre or post-processing steps. Here, we have attempted to stabilize the sillenite structure by doping 10% Gd and 10% Cr at Bi and Fe sites, respectively. The structural, morphological, optical, and magnetic properties of the as-synthesized compounds were critically analyzed using relevant advanced techniques. The photocatalytic activity was evaluated by the degradation of dyes rhodamine B (RhB), methylene blue (MB), and antibiotic ciprofloxacin (CIP) under solar illumination. Along with industrial dyes, the photocatalytic activity of the as-synthesized photocatalysts toward antibiotic degradation was worthwhile, considering their severe harmful effect on the environment, human health, and the food chain.[1] Lastly, a tentative photocatalytic reaction mechanism has also been systematically explored.

RESULTS AND DISCUSSION

Structural and Morphological Analyses. Figure 1a–c shows the Rietveld refined XRD patterns of S-BFO compounds synthesized at 120, 140, and 160 °C hydrothermal reaction temperatures, which have been denoted as S-BFO(120), S-BFO(140), and S-BFO(160), respectively, to facilitate the description.

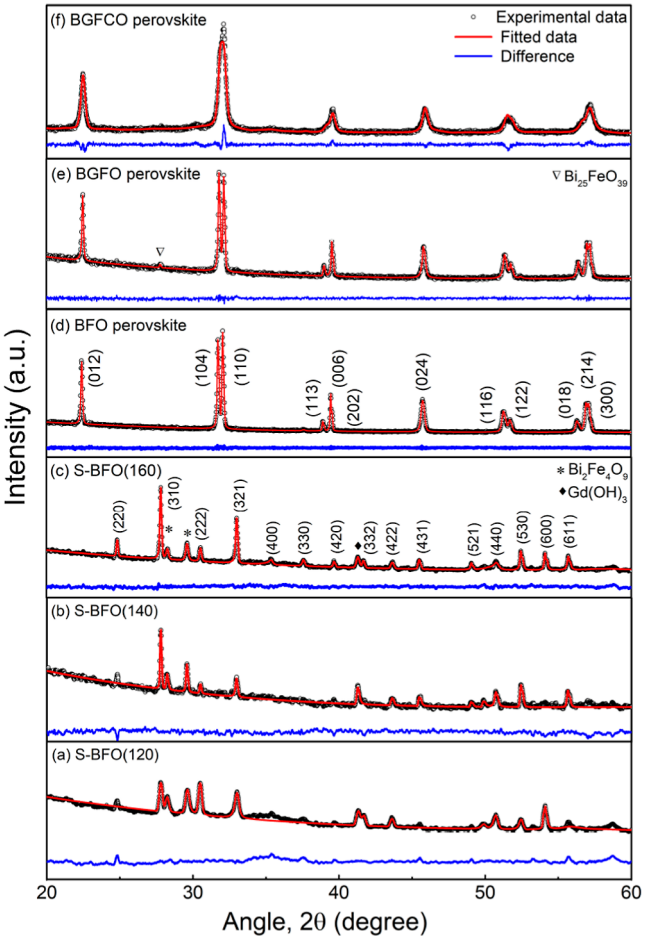

Figure 1. XRD patterns of S-BFO samples at (a) 120, (b) 140, and (c) 160 °C reaction temperatures, respectively; XRD patterns of (d) BFO, (e) BGFO, and (f) BGFCO perovskites from previous investigations[11,30] are included for comparison.

For optimization, we have also recorded the XRD data for samples synthesized at 180 and 200 °C reaction temperatures, included in the Supporting Information Figure S1. As observed from these patterns, above 160 °C temperatures, the crystal structures have almost deteriorated. Therefore, the Rietveld refinement was conducted on the compounds within the 120–160 °C reaction temperature range. Diffraction peaks for all the S-BFO compounds, as shown in Figure 1, matched well with JCPDS card no. 0046-0416 and are indexed as $Bi_{25}FeO_{40}$ with the body-center cubic structure (space group-*I*23).[13] However, a few impurity phases of $Bi_2Fe_4O_9$ and $Gd(OH)_3$ were also observed, which is very obvious during synthesis at such low

https://doi.org/10.1021/acsomega.2c03457
ACS Omega 2022, 7, 34901–34911

reaction temperatures.[27,29] In a previous investigation,[22] the authors observed that without any rare earth dopant, sillenite-type $Bi_{12.5}Fe_{0.5}O_{19.5}$ was formed at 120 and 140 °C reaction temperatures, with the presence of several impurity peaks of Bi_2O_3 and $Bi_2Fe_4O_9$ phases. Also, the sillenite structure was not stable. Notably, for comparative analysis, XRD data from previous investigations[11,30] on undoped, mono-doped, and co-doped BFO have been included in Figure 1d–f. In our recent investigation,[11] doping with 10% Gd in the bismuth site at 160 °C hydrothermal reaction temperature resulted in the formation of perovskite BFO. Moreover, in another investigation,[30] the authors demonstrated that co-doping of Gd and Cr in BFO, followed by the chemical solution deposition technique at high calcination temperature (600 °C), resulted in the formation of mixed-phase perovskite BFO. Surprisingly, in the present investigation, we have succeeded to form sillenite BFO by substituting 10% Gd in the Bi site along with the substitution of 10% Cr in the Fe site. It can be anticipated that the ionic size mismatch of cations in co-substituted BFO resulted in lattice distortion, which favored the formation of a sillenite structure rather than a perovskite one. Such structural deformation due to co-doping has also been reported in several previous investigations.[9,31,32]

The FTIR spectra of all the synthesized samples were recorded at room temperature to further evaluate the formation mechanism of the S-BFO samples. As show in Figure 2, the peaks within 400–600 cm^{-1} agree well with the

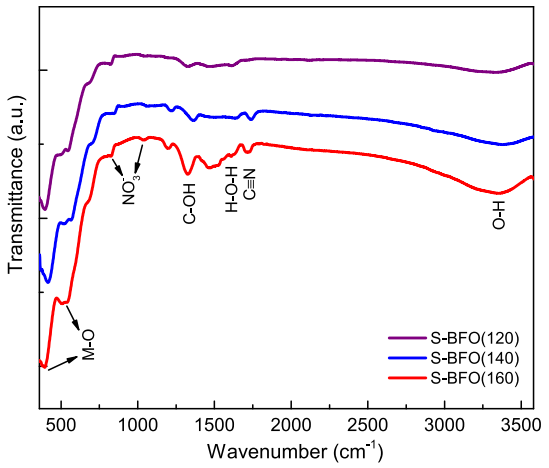

Figure 2. Room temperature FTIR spectra of S-BFO samples synthesized at different reaction temperatures.

characteristic peaks of cubic sillenite[27] and are assigned to the Bi–O bending and Fe–O stretching vibrations.[28] The bands around 850 and 1050 cm^{-1} are due to the presence of NO_3^- on the surface of the sample.[33] The band near 1330 cm^{-1} is attributed to the C-OH stretching vibration.[28] The bands in the region of 1400–1500 cm^{-1} indicate the existence of organic compounds (like ethanol) may be due to residual during the washing process. The bands near 3000–3600 cm^{-1} may be assigned to the O–H stretching, and the peak at 1634 cm^{-1} is attributed to H–O–H stretching of the adsorbed water molecules.[28] Also, the peaks at 1600–1700 cm^{-1} may correspond to nitrile.[34] In the spectra of the compounds with different reaction temperatures, some shifting in modes along with the change in intensity of peaks in comparison with each other have been observed, which can be explained in terms of the existence of internal stresses in the samples and lattice distortions.[34]

The morphological analysis of the synthesized samples was initially conducted by FESEM imaging, as shown in Figure 3a–

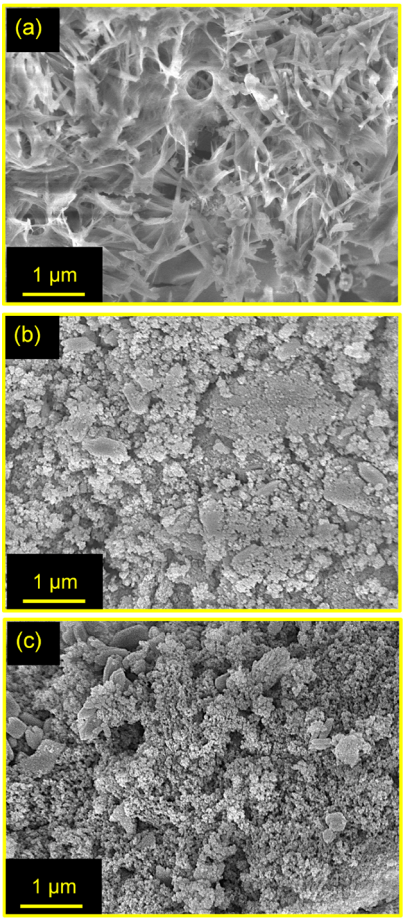

Figure 3. FESEM images of (a) S-BFO(120), (b) S-BFO(140), and (c) S-BFO(160) samples.

c. The effect of hydrothermal reaction temperature on the morphology can be clearly observed from the figures. At 120 °C reaction temperature, as the temperature was too low, the crystal nucleation of S-BFO(120) could not grow completely during the reaction process, and we have obtained a combination of rod and particle-like morphology. As the temperature increases, the thermodynamic mechanism was in the favor of the formation of nanoparticles. The S-BFO powder synthesized at 140 °C reaction temperature displayed agglomerated nature, consisting of nanoparticles of irregular shape. Such an agglomeration phenomenon suggests that the elemental growth of bismuth followed the growth mechanism of nucleation and agglomeration.[35] At 160 °C reaction temperature, the morphology is almost similar to that of the S-BFO(140) sample, though the agglomeration was comparatively reduced. Moreover, the energy dispersive X-ray spectroscopy (EDX) analysis was also performed with a view to determining the elemental composition of synthesized S-BFO(160) nanoparticles. Supporting Information Table S1 demonstrates the measured mass and atomic percentages of all the elements in the representative sample.

To gather more detailed information about the microscopic morphology and the crystalline structure of S-BFO com-

https://doi.org/10.1021/acsomega.2c03457
ACS Omega 2022, 7, 34901–34911

pounds, TEM images of the representative sample S-BFO(160) were captured (Figure 4). Based on the favorable

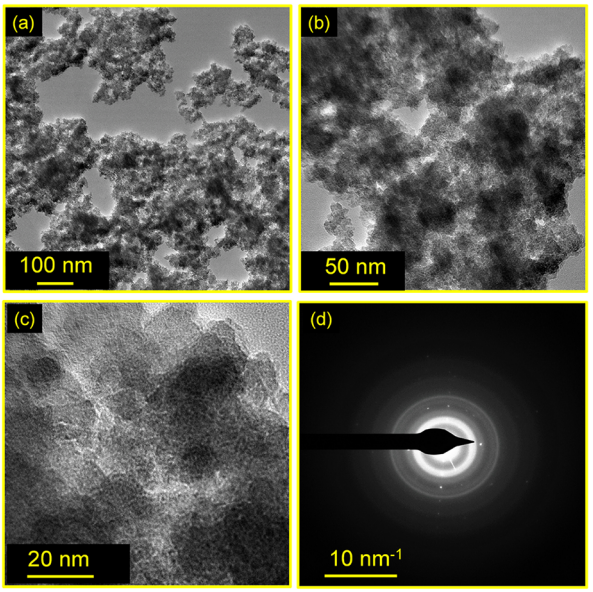

Figure 4. (a–c) Low to high magnification TEM images and (d) corresponding SAED pattern of S-BFO(160).

crystal structure, as observed from the Rietveld analysis, the sample S-BFO(160) was selected to be further analyzed, following TEM and HRTEM. As shown in Figure 4a–c, the sample displays micron-scale plate structures assembled by dozens of nanometer particles.[35] The SAED image in Figure 4d indicates the polycrystalline nature of these nanoparticles. TEM imaging also ensured that S-BFO(160) powders are composed of nanoparticles, as was also observed from FESEM imaging.

Chemical States. XPS measurements were carried out on a representative sample, S-BFO(160), to learn about the chemical composition and valence states of its elements. The full survey spectra in Figure 5a validate the inclusion of Gd and Cr in the S-BFO structure. In Figure 5b, the Gd-3d spectra show two peaks centered at 1187.5 and 1219.1 eV, corresponding to the spin–orbit splitting of $3d_{5/2}$ and $3d_{3/2}$ energy levels with an energy difference of about 32 eV. These findings agree with the reports obtained for $Gd(OH)_3$.[36,37] The deconvolution of each Cr-$2p_{3/2}$ and Cr-$2p_{1/2}$ peak (Figure 5c) corresponds to higher and lower binding energy peaks, thereby suggesting the appearance of Cr in multiple states in the S-BFO(160) sample.[38] Such an appearance of at least two nonequivalent oxidation states in Cr-doped sillenite crystals, for example, $Bi_{12}SiO_{20}$ and $Bi_{12}TiO_{20}$ has also been reported previously.[39] Figure 5d–f demonstrates the high-resolution Bi-4f, Fe-2p, and O-1s XPS spectra of the sample. The Bi-4f narrow scan spectra can be decomposed into two peaks. One peak centered at 158.5 eV can be indexed to the Bi-$4f_{7/2}$ and another at 163.8 eV is ascribed to Bi-$4f_{5/2}$, thereby confirming the presence of the Bi in the trivalent state in the sample. In Figure 5e, for the Fe-2p orbital, the doublets Fe-$2p_{3/2}$ and Fe-$2p_{1/2}$ occur due to spin–orbit splitting. By the deconvolution of the Fe-$2p_{3/2}$ peak, two peaks were observed. The 709.5 eV peak belongs to Fe^{2+}, while the peak at 711.1 eV corresponds to the Fe^{3+} valance state and thus manifests the existence of

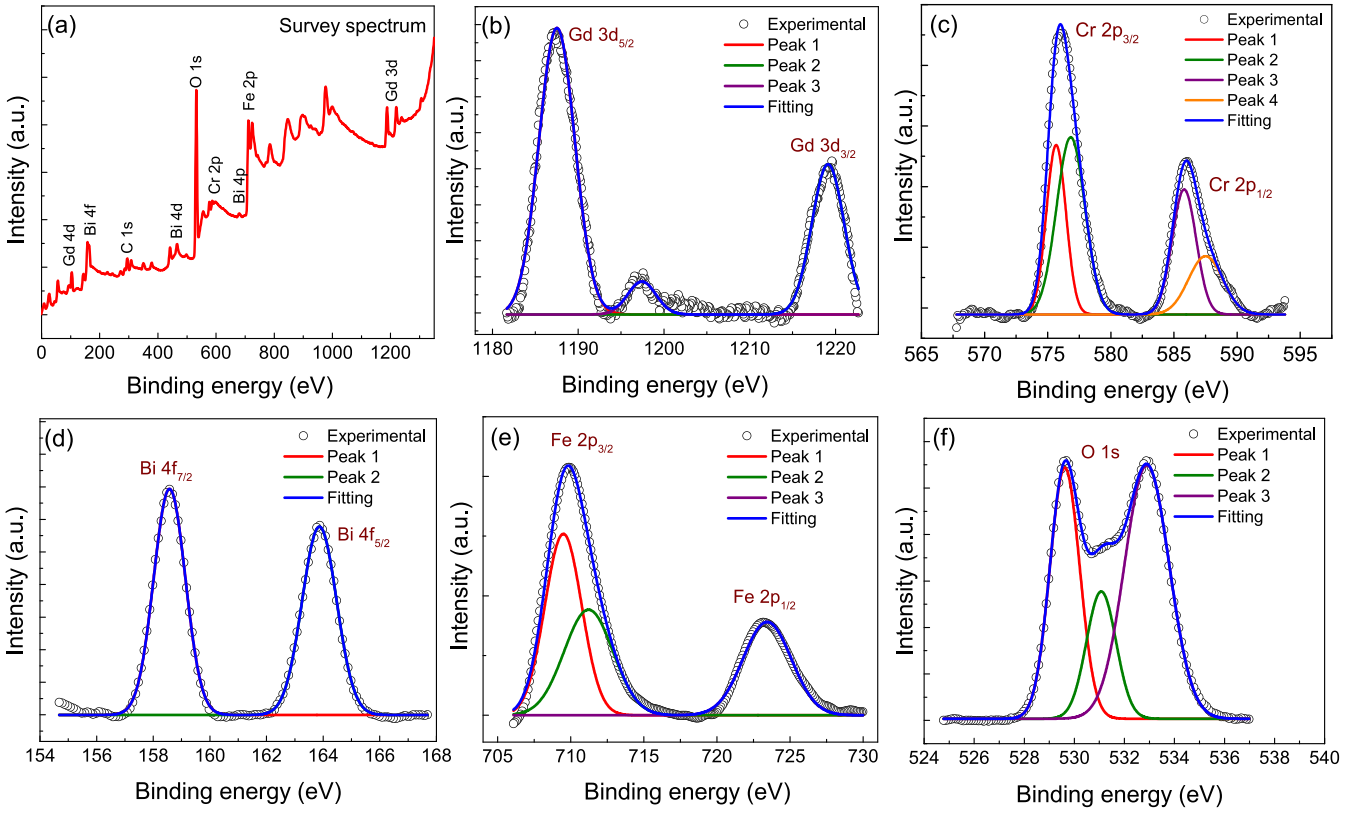

Figure 5. XPS full survey spectrum (a); narrow scan spectra of (b) Gd-3d, (c) Cr-2p, (d) Bi-4f, (e) Fe-2p, and (f) O-1s for the S-BFO(160) sample.

https://doi.org/10.1021/acsomega.2c03457
ACS Omega 2022, 7, 34901–34911

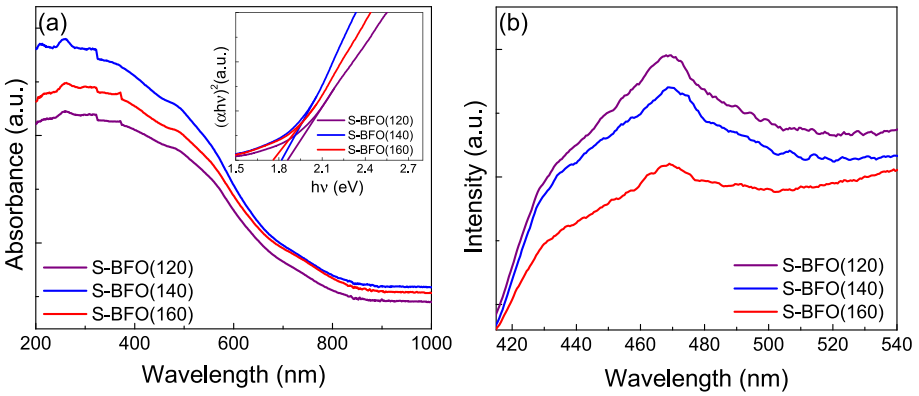

Figure 6. (a) UV−visible spectra; Tauc plots for band gap estimation in the inset and (b) steady-state PL spectra of S-BFO samples.

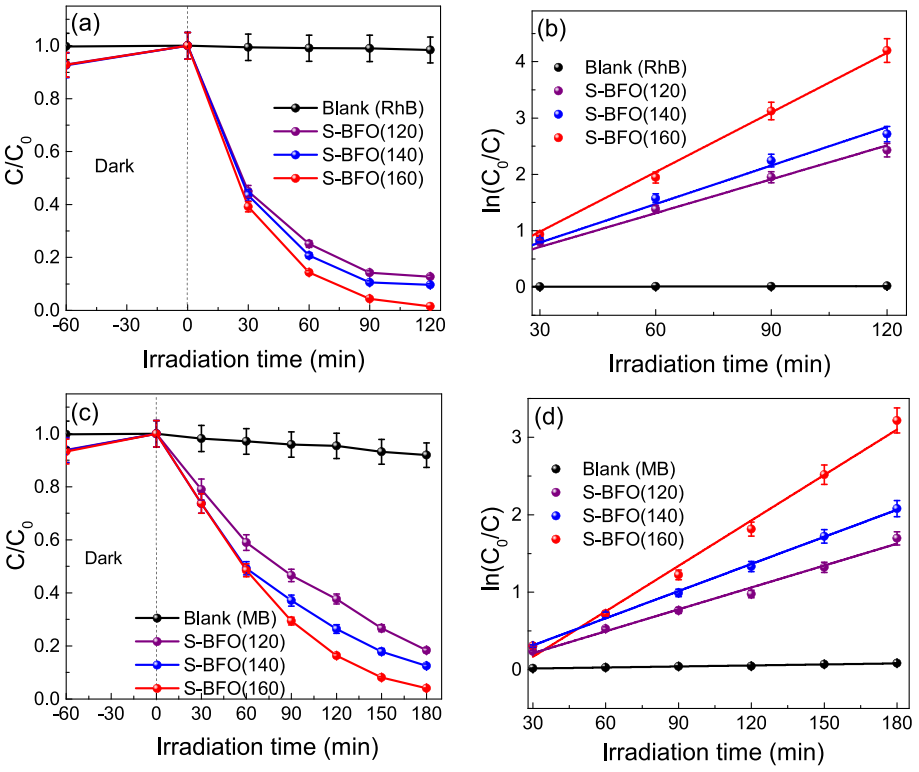

Figure 7. Changes in the concentration of (a) RhB and (c) MB vs irradiation time and first-order kinetics of photodegradation of (b) RhB and (d) MB using different S-BFO samples.

both divalent and trivalent states of Fe in the S-BFO(160) sample.[11] The O-1s spectra (Figure 5f) have been deconvoluted and fitted with three peaks with binding energies centered at 529.6, 531.1, and 532.8 eV, which could be assigned to O^{2-} bound to Bi, oxygen vacancies, and the surface adsorbed hydroxyl group, respectively.[40] The occurrence of the oxygen vacancies may promote the separation of photo-generated charge carriers, enhancing the properties of the photocatalyst.[41]

Optical Characterization. The optical properties of the synthesized samples were evaluated by UV−vis DRS and steady-state PL spectroscopy analyses. Following the Kubelka−Munk (K−M) theory, the experimentally obtained UV−vis DRS spectra were converted to the corresponding absorption spectra. As seen in Figure 6a, all the S-BFO samples demonstrated strong and broad absorption in the range of 200−600 nm, which is proven to be beneficial for visible light harvesting and improvement of photocatalytic performance.[12] The band gaps of S-BFO(120), S-BFO(140), and S-BFO(160) were determined to be 1.86, 1.82, and 1.76 eV, respectively, using the plot of $(\alpha h\nu)^2$ versus the photon energy ($h\nu$) (inset of Figure 6a). These band gap values are very close to those of early investigations on sillenite-type bismuth ferrites.[26,27] Moreover, compared to some other sillenite materials such as $Bi_{25}GaO_{39}$, $Bi_{12}GeO_{20}$, $Bi_{12}SiO_{20}$, and $Bi_{24}AlO_{39}$,[17,42−44] the as-synthesized S-BFO samples have a lower energy gap which will give large spectral coverage, implying their potential application in wastewater treatment as promising UV and visible light active photocatalysts. The steady-state PL spectra of all the samples were recorded at room temperature to qualitatively understand the electron−hole pair recombination rate. While looking at Figure 6b, it is clear that the variation in the reaction temperatures during the synthesis of S-BFO has induced a change in the PL intensity, without changing the

https://doi.org/10.1021/acsomega.2c03457
ACS Omega 2022, 7, 34901−34911

emission peak position. However, a strong quenching of the PL intensity for the sillenite BFO compound synthesized at 160 °C reaction temperature is clearly observed, suggesting the lowest recombination rate of the photogenerated charge carriers for S-BFO(160) and hence may greatly influence its photocatalytic properties.[45]

Photocatalytic Performance. The photocatalytic performance of the prepared samples was initially evaluated through the degradation of RhB dye under solar illumination, and the results are presented in Figure 7a,b. Here, C/C_0 is used to quantify the degradation efficiency, where C is the concentration of RhB at any time t, and C_0 is the primary concentration of RhB. It is to be noted that before conducting this photocatalytic experiment, a dark test was performed under constant stirring for about 1 h so that adsorption−desorption conditions could be attained. From Figure 7a, it can be observed that the efficiency of RhB degradation was ∼88% with S-BFO(120) and ∼91% with S-BFO(140) samples, while with S-BFO(160) nanopowders, almost 100% degradation was completed within 120 min of irradiation. Figure 7b displays the illumination time profiles of $\ln(C_0/C)$. The slopes indicate the reaction rate constants and thus intuitively show the photocatalytic activity of the materials. Notably, the degradation efficiency of this co-doped sillenite-phase S-BFO photocatalyst is much higher as compared to the perovskite-phase undoped and mono-doped BFO photocatalysts.[11] This could be due to their super-fine nanopowder-like morphology which remained completely blended within the dye−catalyst mixture throughout the degradation process and destructed the whole conjugated chromophore structure of RhB. The RhB degradation was found to follow the pseudo first-order kinetic model, and the rate constants are 0.02003, 0.02282, and 0.03529 min^{-1} with S-BFO(120), S-BFO(140), and S-BFO(160), respectively (Figure 7b). The rate constant for RhB alone was only 1.50×10^{-4} min^{-1}. It is noteworthy that S-BFO(160) displayed the highest photocatalytic activity compared to the rest.

Photocatalytic degradation of another dye MB was used to further investigate the photocatalytic activity of the synthesized samples, and the results are presented in Figure 7c,d. Under solar illumination, the samples demonstrated very good photocatalytic activity for MB solution, and about 81, 88, and 97% degradation for MB in 180 min was observed with S-BFO(120), S-BFO(140), and S-BFO(160), respectively (Figure 7c). In this case, also, S-BFO(160) showed the highest rate constant of 0.02077 min^{-1}, while without any photocatalyst, the rate constant during MB degradation was 4.36×10^{-4} min^{-1} (Figure 7d). However, MB's degradation rate was lower than that of RhB, which could be due to the presence of stable and bulky aromatic rings in the molecular structure of MB, which might have suppressed the interaction between catalysts and dye molecules.[46] Moreover, the mineralization property of the most efficient photocatalyst (S-BFO(160)) was ensured from the total organic carbon (TOC) measurements. The amount of TOC present in the aqueous solution after complete degradation of the pollutants was found to be ∼0.2 mg/L which is much lower than the acceptable level of TOC (2−4 mg/L) in the treated/drinking water.[47]

Decomposition of a colorless pollutant, CIP, using S-BFO compounds was also performed to monitor the occurrence of dye sensitization phenomena under simulated solar irradiation.[11] The characteristic absorbance peak of CIP was observed at 276 nm, and the corresponding intensity of the UV−vis absorption spectra decreased over time, demonstrating the photocatalytic degradation of CIP. As seen in Figure 8,

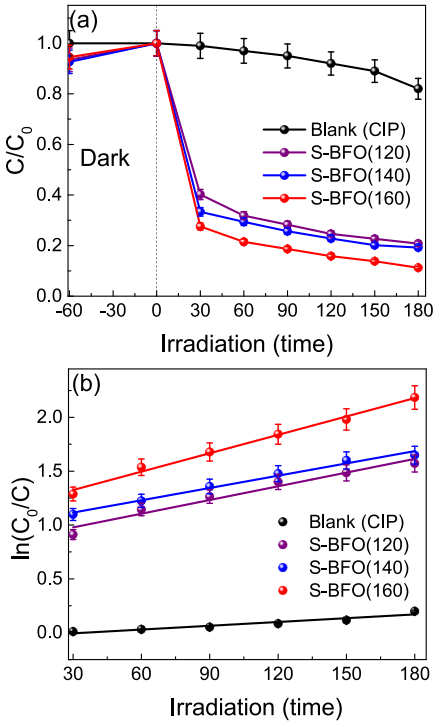

Figure 8. (a) Plot of changes in the CIP concentration and (b) pseudo-first order kinetics for CIP photodegradation, with and without using S-BFO photocatalysts.

among all the samples, the S-BFO(160) photocatalyst demonstrated the highest efficiency (89%) and rate constant (0.0057 min^{-1}) during CIP degradation within 180 min of solar irradiation. These results clearly show that the RhB and MB dye degradation were related to the photocatalytic performance of the as-synthesized photocatalysts rather than dye sensitization, as the colorless CIP is unable to sensitize a photocatalytic reaction under solar illumination.[48,49]

Stability and Scavenging Experiments. Reusability and stability are two crucial factors for the large-scale industrial application of photocatalysts for pollutant degradation.[11] The cyclic performances of the S-BFO(160) compound are shown in Figure 9a,b, demonstrating five consecutive cycles of RhB and CIP degradation. Nominal changes in the photocatalytic activities were observed after five cycles, implying satisfactory stability with good recycling ability of this photocatalyst. The structural stability was further confirmed by XRD analysis, which demonstrated no structural deterioration in the S-BFO(160) photocatalyst after five cycles of recycling (Figure 9c).

The active species trapping tests were conducted using the S-BFO(160) sample to evaluate the most responsible species for RhB dye degradation. During organic pollutant degradation, different reactive species including h^+ (holes), $^{\bullet}O_2^-$ (superoxide radical), and $^{\bullet}OH$ (hydroxyl radical) are involved in the photocatalytic reactions. From Figure 9d, it is observed that the introduction of acrylamide ($^{\bullet}O_2^-$ scavenger) into the reaction medium had a minimal effect on the photocatalytic degradation of RhB. On the contrary, when EDTA-2Na (h^+ scavenger) was induced, the degradation efficiency was

https://doi.org/10.1021/acsomega.2c03457
ACS Omega 2022, 7, 34901−34911

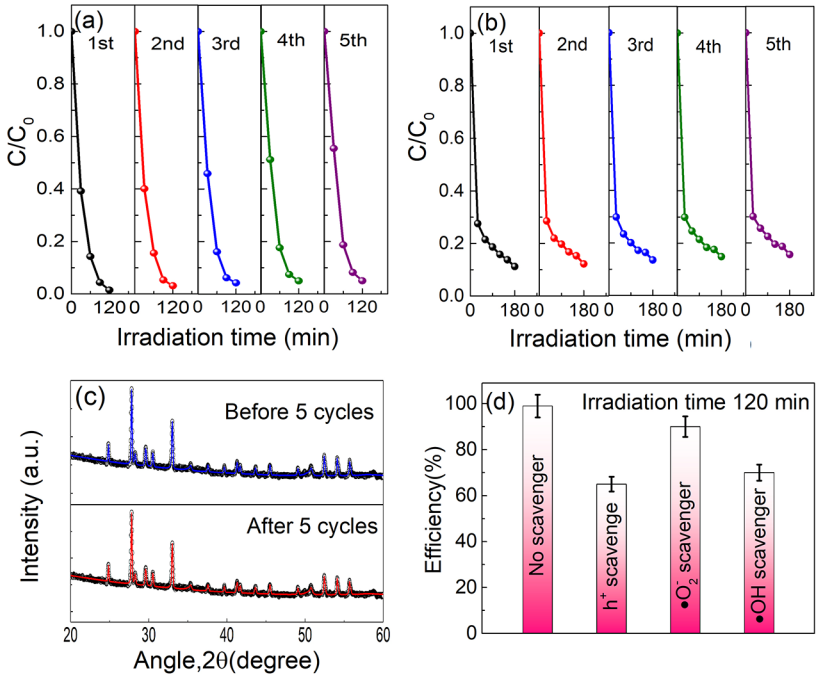

Figure 9. Reusability test toward (a) RhB and (b) CIP degradation during five successive runs, (c) XRD patterns before and after five consecutive cycles of photocatalysis, and (d) active species trapping experiment for the S-BFO(160) sample.

Table 1. Overview of Pollutant Degradation Ability of Sillenite-Phase BFO Photocatalysts in Previous Investigations

composition	method (temp.)	pollutant	light source	time (min.)	degradation (%)	reference
$Bi_{25}FeO_{40}$	hydrothermal (200 °C, 6 h)	methyl orange	500 W Xe lamp	420	84	50
$Bi_{25}FeO_{40}$	hydrothermal (120−200 °C, 24 h)	rhodamine B	500 W halogen lamp	180	99 (180 °C sample)	21
$Bi_{25}FeO_{40}$	hydrothermal (180 °C, not mentioned)	rhodamine B	500 W Xe lamp	240	62	12
$Bi_{36}Fe_2O_{57}$	solvothermal (150 °C, 12 h)	rhodamine B	300 W Xe lamp	60	9.3	35
$Bi_{25}FeO_{40}$	hydrothermal (180 °C, 12 h)	rhodamine B	500 W Xe lamp	300	13	27
$Bi_{25}FeO_{40}$	molten-salt growth (650 °C, 2 h)	rhodamine B	250 W Xe lamp	240	30	26
$Bi_{12}FeO_{20}$	hydrothermal (200 °C, 72 h)	congo red	natural sunlight	210	32.10	51
		methylene blue		210	74.23	
$Bi_{25}FeO_{40}$	hydrothermal (160 °C, 6 h)	rhodamine B	500 W Hg Xe lamp	120	99	present study
		methylene blue		180	97	
		ciprofloxacin		180	89	

significantly decreased, indicating that holes were the principal reactive species accountable for the photocatalytic activity. The addition of IPA (•OH scavenger) also demonstrated a reduction in the degradation rate, indicating the contribution of •OH to the degradation mechanism.

Comparative Analysis of the Photocatalytic Performance. In Table 1, we have presented a comparative analysis of the photocatalytic performance of our most efficient photocatalyst, S-BFO(160), with few previous relevant investigations on sillenite-phase BFO compounds. Notably, the photocatalytic ability of photocatalysts depends strongly on experimental parameters; hence, for comparison, the relevancy of the parameters was considered as much as possible. Nevertheless, among all the samples tabulated here, S-BFO(160) showed the highest efficiency with almost complete degradation of RhB and MB dye within 120 and 180 min of solar irradiation. Moreover, most studies presented here on photocatalytic performance of sillenite BFO samples evaluated the photocatalytic activity of the photocatalyst by the degradation of colored dye alone, which is known to sensitize a photocatalytic reaction.[51,52] However, in our experiment, along with colored dyes, we have examined the photocatalytic properties of our synthesized samples through the degradation of colorless antibiotic, which indicated that the degradation is purely photocatalytic, not dye-sensitized.[11,48] Though in most of the earlier studies, the sillenite BFO samples were synthesized following a facile solvothermal or hydrothermal reaction route, the process was very time-consuming, and the photocatalytic activity was not very promising.[27,35] However, in the present investigation, we were able to produce sillenite-structured BFO within 6 h at a very lower reaction temperature of 140−160 °C without any sort of pre/post-processing time and energy consuming steps. Moreover, in earlier investigations on the photocatalytic performance of both sillenite- and perovskite-phase BFO, the presence of H_2O_2 in the reaction medium has been observed to facilitate the pollutant degradation rate, which is not preferable from the eco-friendly point of view.[26,53] However, in the present investigation, we have observed very good pollutant deterioration efficiency of our synthesized photocatalyst without introducing any toxic reagent in the reaction medium. Hence, it can be anticipated that these smaller sized S-BFO(160) particles with high surface

https://doi.org/10.1021/acsomega.2c03457
ACS Omega 2022, 7, 34901−34911

to volume ratio have resulted in improving the activity of the photocatalyst by absorbing significant number of photons from the solar spectrum and creating electron−hole pairs to take part in the degradation reaction. The high photocatalytic performance also gets support from PL analysis, which revealed the suppression of charge carrier recombination due to the inclusion of dopants into the BFO structure.[11]

Photocatalytic Mechanism. To investigate the profound photocatalytic performance of the sillenite bismuth ferrite samples, the band edge potentials of the S-BFO(160) photocatalyst were identified with the help of the Mulliken electronegativity formula.[54] These band edges play a crucial role in understanding the separation, generation, and passage of the photogenerated charge carriers throughout the degradation process. The valence band (VB) and conduction band (CB) edges were calculated using the following equations[48]

$$E_{VB} = \chi - E_0 + \frac{1}{2}E_g \quad (1)$$

$$E_{CB} = E_{VB} - E_g \quad (2)$$

Here, the CB and VB edge potentials are denoted by E_{CB} and E_{VB}, respectively; χ represents the absolute electronegativity of a semiconductor, and for the sillenite BFO structure, the value is 6.24 eV; E_0 is the energy of free electrons on the hydrogen scale (∼4.5 eV) and E_g is the band gap energy [1.76 eV vs NHE for S-BFO(160)], respectively. Therefore, the E_{VB} and E_{CB} values were calculated to be 2.62 and 0.86 eV, respectively, which match well with a previous study.[55] Based on these calculations and results of active species trapping experiments on the S-BFO(160) sample, a schematic diagram for the photocatalytic mechanism toward RhB degradation is proposed in Figure 10.

Upon solar irradiation with the energy of photon equal to or greater than the band gap of S-BFO, the electrons (e^-) in the VB receive the energy and get transferred from the VB to the CB, which results in the creation of holes in the VB and electrons in the CB. The holes accumulated at the VB may directly degrade the RhB molecules, as shown in eq 4, or/and may combine with adsorbed H_2O molecules on the photocatalyst surface and generate $^{\bullet}OH$ as the VB potential (2.62 eV) is more positive than that of $^{\bullet}OH/H_2O$ (2.38 eV).[55] These hydroxyl radicals will also take part in the decomposition of RhB into less harmful by-products, followed by the production of H_2O and CO_2. However, the electrons in the CB of the photocatalyst are not able to absorb dissolved O_2 to produce $^{\bullet}O_2^-$ that can oxidize RhB as the CB potential (0.86 eV) is more positive than the $O_2/^{\bullet}O_2^-$ redox potential (−0.32 eV).[55] Thus the degradation mechanism is mainly governed by H^+ and $^{\bullet}OH$, rather than by $^{\bullet}O_2^-$, which is also consistent with our findings from the active species trapping experiments.

The following is the proposed mechanism for the photodegradation of RhB dye molecules

$$\text{S-BFO} + h\nu \rightarrow \text{S-BFO}\ (e^- + h^+) \quad (3)$$

$$h^+ + \text{Dye} \rightarrow \text{degraded products} \quad (4)$$

$$h^+ + H_2O \rightarrow {}^{\bullet}OH \quad (5)$$

$$\text{Dye} + {}^{\bullet}OH \rightarrow \text{degraded products} \quad (6)$$

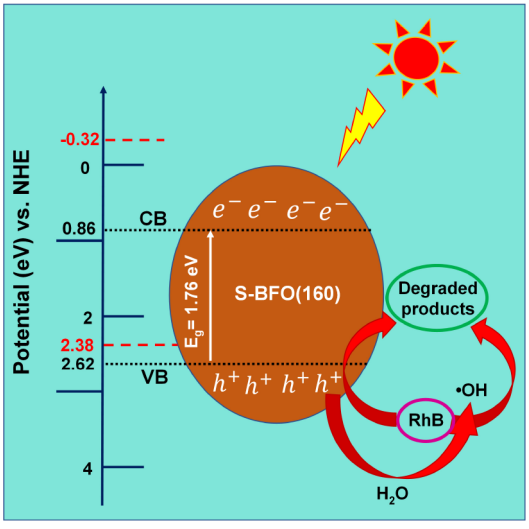

Figure 10. Schematic charge transfer mechanism in the photodegradation of RhB dye by the S-BFO(160) photocatalyst under solar irradiation.

Magnetic Characterization. Along with its photocatalytic properties, the potential application of a photocatalyst depends on its efficient separation from the solution medium. If the photocatalyst possesses magnetic properties, it is expected to be easily separable using a magnetic field. To explore such characteristics in the as-synthesized photocatalysts, the magnetization versus magnetic field (M-H) hysteresis loops of two powder samples S-BFO(140) and S-BFO(160) were measured at room temperature, as can be seen in Figure 11.

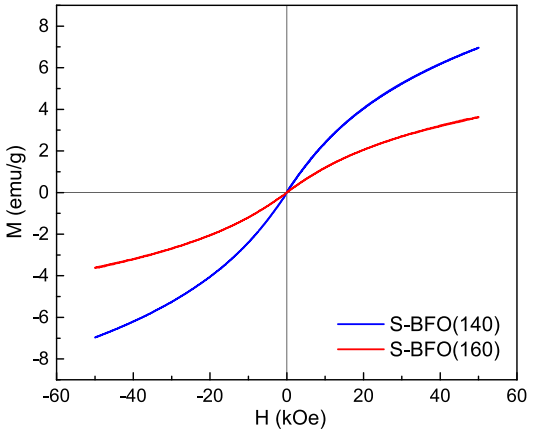

Figure 11. Room temperature M-H loops of S-BFO(140) and S-BFO(160) photocatalysts.

The magnetic behavior of the S-BFO(120) sample was not studied as the sillenite structure was not completely formed in this sample, and also, the morphology was irregular. The maximum magnetization at 50 kOe is 6.97 and 3.63 emu/g for S-BFO(140) and S-BFO(160) samples, respectively. Such a high magnetization value of S-BFO(140) is probably associated with the higher secondary phases present in the sample, which were not detected by the XRD technique due to its limit of detection.[9,19,56] This observation also suggests that our desired photocatalyst with a better sillenite structure is S-BFO(160) compared to that of S-BFO(120) and S-BFO(140).

A careful observation of the shape of the room temperature M-H loops of the as-synthesized S-BFO(140) and S-

https://doi.org/10.1021/acsomega.2c03457
ACS Omega 2022, 7, 34901−34911

BFO(160) samples indicates a superposition of their paramagnetic and superparamagnetic nature, arising mainly from sillenite and some other phases.[56] To identify these phases and investigate their comprehensive role on magnetic behavior, further investigation is required. Nevertheless, we have observed the difference in room temperature magnetic behavior of our sillenite-type bismuth ferrite samples synthesized by co-doping of Gd and Cr to that of a perovskite phase Dy and Cr co-doped bismuth ferrite sample.[57] In their investigation, Mao et al. synthesized Dy and Cr co-doped BFO through a sol−gel technique and observed the formation of a perovskite phase BFO. The room temperature M-H loops of these samples demonstrated a wider loop at the center of the hysteresis, which is clearly different from that of our sillenite-phase powder samples, for which we did not observe any wider central loop. Therefore, based on our XRD and magnetization measurement, we can confirm the formation of sillenite-phase bismuth ferrite by a low temperature hydrothermal technique via the co-doping approach. The promising magnetic behavior of the as-synthesized S-BFO sample might be beneficial for the recovery of the catalysts from the catalytic reaction medium.

CONCLUSIONS

We have demonstrated a simple technique to fabricate sillenite-type $Bi_{25}FeO_{40}$ at a very low reaction temperature. Co-doping of 10% Gd and 10% Cr at the Bi and Fe sites of BFO disclosed a structural phase transformation of BFO from perovskite to sillenite by tuning the hydrothermal reaction temperatures for a fixed reaction time of only 6 h. The formation of the sillenite phase was confirmed by XRD and magnetization measurements. Sillenite compounds synthesized at reaction temperatures ranging from 120 to 160 °C exhibited promising photocatalytic performance toward the degradation of RhB, MB, and CIP. More specifically, the sillenite-type $Bi_{25}FeO_{40}$ synthesized at 160 °C displayed higher photocatalytic efficiency compared to other synthesized compounds, as well as undoped, and mono-doped perovskite BFO synthesized under similar hydrothermal conditions. Such profound performance of S-BFO(160) could be imputed to its nanopowder-like morphology, relatively small band gap (1.76 eV), and suppressed charge carrier recombination phenomena. According to active species trapping experiments, holes and hydroxyl radicals played the principal roles in the photocatalytic reaction. On this basis, a plausible charge transfer mechanism has been proposed. From an economic perspective, such an energy-efficient production of the sillenite bismuth ferrite photocatalyst is appealing, and it shows potential to be used in purifying contaminated water supplies.

EXPERIMENTAL SECTION

Sample Preparation. In a typical procedure, stoichiometric amounts of bismuth nitrate pentahydrate ($Bi(NO_3)_3 \cdot 5H_2O$), iron nitrate nonahydrate ($Fe(NO_3)_3 \cdot 9H_2O$), gadolinium nitrate hexahydrate ($Gd(NO_3)_3 \cdot 6H_2O$), and chromium nitrate nonahydrate ($Cr(NO_3)_3 \cdot 9H_2O$), along with 10 M KOH, were dissolved in 50 mL of deionized (DI) water. The obtained suspension was stirred for 4 h at ambient temperature. The solution was then transferred into a 100 mL Teflon lined stainless steel autoclave, and the sealed reactor was heated for 6 h at different hydrothermal reaction temperatures (120−200 °C). The final products were washed with DI water and ethanol several times, then dried at 80 °C for 10 h, and the bismuth ferrite samples at different reaction temperatures were obtained. The 10% Gd and 10% Cr concentration were chosen based on some previous investigations on $BiFeO_3$ conducted by our group.[9,11] Supporting Information Figure S2 schematically shows the hydrothermal synthesis steps of the S-BFO compound at 160 °C reaction temperature.

Characterization. The structural characteristics of the as-prepared samples were analyzed by X-ray diffraction (XRD, Rigaku SmartLab) with Cu radiation Kα (0.15406 nm). SmartLab Studio 2 software was utilized for phase identification. Fourier transform infrared (FTIR) spectra of all the samples were collected using a Spectrum Two FT-IR spectrometer (PerkinElmer). The surface morphology of the as-synthesized powder samples was analyzed by a field emission scanning electron microscope (JEOL, JSM-7600F, Japan). Furthermore, a transmission electron microscope (Talos F200X, Thermo fisher scientific, USA) was employed for extensive morphological analysis. A Kα X-ray photoelectron spectrometer (Thermo Fisher Scientific) was used to study the valence states of all elements in the compounds. The optical properties of the samples were investigated from the diffused reflectance spectra, using an ultraviolet−visible (UV−vis) spectrophotometer (UV-2600; Shimadzu, Japan). A Spectro fluorophotometer (RF-6000; Shimadzu, Japan) was employed to conduct steady-state photoluminescence (PL) spectroscopy to explore the electron−hole recombination rate during the photocatalytic reactions. The room temperature magnetic hysteresis (M-H) loops were measured using a physical property measurement system (PPMS).

Photocatalytic Activity. Photocatalytic performances of the as-synthesized photocatalysts were assessed following the degradation of cationic dyes such as RhB and MB and a colorless antibiotic CIP under solar irradiation.[11] Photocatalytic activities were conducted in a glass beaker under continuous magnetic stirring to keep the dye and catalyst mixture homogeneously distributed in the solution. A 50 mL dye solution (12 mg/L) that contained 40 mg of the as-synthesized S-BFO photocatalyst was taken in a beaker and was stirred in the dark for about an hour so that adsorption−desorption conditions could be achieved. Then, the photocatalytic tests were performed at room temperature under solar illumination using a 500 W Hg Xe lamp (irradiance power density = 100 mW cm^{-2}) as a solar simulator.[58] A schematic photocatalytic reactor setup for the pollutant degradation experiments has been depicted in Supporting Information Figure S3. During the photocatalytic reaction, after equal intervals of time, a sufficient amount of solution was taken from the beaker, the catalyst was separated from the dye solution by centrifugation, and the dye solution was analyzed using a UV−vis spectrophotometer. The separated photocatalyst after each experiment was collected, washed with DI water, dried, and used again for the reusability test. The pH of the solution was maintained at around 3. For the degradation of antibiotic CIP, 15 mg of the photocatalyst was mixed in 50 mL of DI water at neutral pH, and the concentration of CIP was 10 mg/L, and the rest of the procedures were similar to those for dye. The amount of the total organic carbon (TOC) was determined with a TOC analyzer (Shimadzu, Japan), according to method 5310B.

Active species trapping experiments were carried out following the similar photocatalytic procedure with the addition of scavengers, namely, isopropyl alcohol (IPA), acrylamide, and disodium ethylenediamine tetraacetic acid

https://doi.org/10.1021/acsomega.2c03457
ACS Omega 2022, 7, 34901−34911

(EDTA-2Na) into the RhB solution to trap hydroxyl radicals, superoxide radicals, and holes, respectively.[48]

■ ASSOCIATED CONTENT

Supporting Information

The Supporting Information is available free of charge at https://pubs.acs.org/doi/10.1021/acsomega.2c03457.

XRD patterns of S-BFO compounds synthesized at 120−200 °C reaction temperatures; Mass and atomic percentages of S-BFO(160) nanoparticles as obtained from EDX analysis.; schematically, the synthesis steps of the S-BFO(160) compound prepared by the hydrothermal technique; and schematically, a photocatalytic reactor setup for the pollutant degradation experiments (PDF)

■ AUTHOR INFORMATION

Corresponding Author

M. A. Basith − *Nanotechnology Research Laboratory, Department of Physics, Bangladesh University of Engineering and Technology, Dhaka 1000, Bangladesh;* orcid.org/0000-0003-4632-0141; Email: mabasith@phy.buet.ac.bd

Author

Fahmida Sharmin − *Nanotechnology Research Laboratory, Department of Physics, Bangladesh University of Engineering and Technology, Dhaka 1000, Bangladesh;* orcid.org/0000-0003-2845-1121

Complete contact information is available at: https://pubs.acs.org/10.1021/acsomega.2c03457

Notes

The authors declare no competing financial interest.

■ ACKNOWLEDGMENTS

We sincerely acknowledge Committee for Advanced Studies and Research (CASR), Bangladesh University of Engineering and Technology for financial assistance.

■ REFERENCES

(1) Qin, K.; Zhao, Q.; Yu, H.; Xia, X.; Li, J.; He, S.; Wei, L.; An, T. A review of bismuth-based photocatalysts for antibiotic degradation: Insight into the photocatalytic degradation performance, pathways and relevant mechanisms. *Environ. Res.* **2021**, *199*, 111360.

(2) Sayed, M.; Khan, A.; Rauf, S.; Shah, N. S.; Rehman, F.; A. Al-Kahtani, A.; Iqbal, J. A.; Boczkaj, J.; Gul, G.; Bushra, I.; Bushra, M. Bismuth-doped nano zerovalent iron: A novel catalyst for chloramphenicol degradation and hydrogen production. *ACS Omega* **2020**, *5*, 30610−30624.

(3) Margha, F. H.; Radwan, E. K.; Badawy, M. I.; Gad-Allah, T. A. Bi_2O_3-$BiFeO_3$ Glass-Ceramic: Controllable β-/γ-Bi_2O_3 Transformation and Application as Magnetic Solar-Driven Photocatalyst for Water Decontamination. *ACS Omega* **2020**, *5*, 14625−14634.

(4) Sayed, M.; Ren, B.; Ali, A. M.; Al-Anazi, A.; Nadagouda, M. N.; Ismail, A. A.; Dionysiou, D. D. Solar light induced photocatalytic activation of peroxymonosulfate by ultra-thin Ti^{3+} self-doped Fe_2O_3/TiO_2 nanoflakes for the degradation of naphthalene. *Appl. Catal., B* **2022**, *315*, 121532.

(5) Ghumro, S. S.; Lal, B.; Pirzada, T. Visible-Light-Driven Carbon-Doped TiO_2-Based Nanocatalysts for Enhanced Activity toward Microbes and Removal of Dye. *ACS Omega* **2022**, *7*, 4333−4341.

(6) Habibi-Yangjeh, A.; Asadzadeh-Khaneghah, S.; Feizpoor, S.; Rouhi, A. Review on heterogeneous photocatalytic disinfection of waterborne, airborne, and foodborne viruses: can we win against pathogenic viruses? *J. Colloid Interface Sci.* **2020**, *580*, 503−514.

(7) Akhundi, A.; Badiei, A.; Ziarani, G. M.; Habibi-Yangjeh, A.; Muñoz-Batista, M. J.; Luque, R. Graphitic carbon nitride-based photocatalysts: toward efficient organic transformation for value-added chemicals production. *Mol. Catal.* **2020**, *488*, 110902.

(8) Asadzadeh-Khaneghah, S.; Habibi-Yangjeh, A. g-C_3N_4/carbon dot-based nanocomposites serve as efficacious photocatalysts for environmental purification and energy generation: A review. *J. Clean. Prod.* **2020**, *276*, 124319.

(9) Basith, M. A.; Kurni, O.; Alam, M. S.; Sinha, B. L.; Ahmmad, B. Room temperature dielectric and magnetic properties of Gd and Ti co-doped $BiFeO_3$ ceramics. *J. Appl. Phys.* **2014**, *115*, 024102.

(10) Sun, M.; Bai, L.; Ma, W.; Liu, Y.; Zhang, J.; Yang, J. Ho and Ti Co-Substitution Tailored Structural Phase Transition and Enhanced Magnetic Properties of $BiFeO_3$ Thin Films. *ACS Omega* **2020**, *5*, 29292−29299.

(11) Sharmin, F.; Basith, M. A. Highly efficient photocatalytic degradation of hazardous industrial and pharmaceutical pollutants using gadolinium doped $BiFeO_3$ nanoparticles. *J. Alloys Compd.* **2022**, *901*, 163604.

(12) Basith, M. A.; Ahsan, R.; Zarin, I.; Jalil, M. A. Enhanced photocatalytic dye degradation and hydrogen production ability of $Bi_{25}FeO_{40}$-rGO nanocomposite and mechanism insight. *Sci. Rep.* **2018**, *8*, 11090.

(13) Jalil, M. A.; Chowdhury, S. S.; Alam Sakib, M.; Enamul Hoque Yousuf, S. M.; Khan Ashik, E.; Firoz, S. H.; Basith, M. A. Temperature-dependent phase transition and comparative investigation on enhanced magnetic and optical properties between sillenite and perovskite bismuth ferrite-rGO nanocomposites. *J. Appl. Phys.* **2017**, *122*, 084902.

(14) Han, J.-T.; Huang, Y.-H.; Wu, X.-J.; Wu, C.-L.; Wei, W.; Peng, B.; Huang, W.; Goodenough, J. B. Tunable synthesis of bismuth ferrites with various morphologies. *Adv. Mater.* **2006**, *18*, 2145−2148.

(15) Xu, S.; Shangguan, W.; Yuan, J.; Shi, J.; Chen, M. Photocatalytic properties of bismuth titanate $Bi_{12}TiO_{20}$ prepared by co-precipitation processing. *Mater. Sci. Eng., B* **2007**, *137*, 108−111.

(16) Lin, X.; Huang, F.; Wang, W.; Shi, J. Photocatalytic activity of $Bi_{24}Ga_2O_{39}$ for degrading methylene blue. *Scr. Mater.* **2007**, *56*, 189−192.

(17) Yao, W. F.; Xu, X. H.; Zhou, J. T.; Yang, X. N.; Zhang, Y.; Shang, S. X.; Wang, H.; Huang, B. B. Photocatalytic property of sillenite $Bi_{24}AlO_{39}$ crystals. *J. Mol. Catal. A: Chem.* **2004**, *212*, 323−328.

(18) Yao, W. F.; Wang, H.; Xu, X. H.; Zhou, J. T.; Yang, X. N.; Zhang, Y.; Shang, S. X.; Wang, M. Sillenites materials as novel photocatalysts for methyl orange decomposition. *Chem. Phys. Lett.* **2003**, *377*, 501−506.

(19) Lopes, A. M.; Araújo, J. P.; Ferdov, S. Room temperature synthesis of $Bi_{25}FeO_{39}$ and hydrothermal kinetic relations between sillenite- and distorted perovskite-type bismuth ferrites. *Dalton Trans.* **2014**, *43*, 18010−18016.

(20) Verma, R.; Chauhan, A.; Neha, K. M.; Batoo, R.; Kumar, M.; Hadhi, E. H.; Raslan, E. H. Effect of calcination temperature on structural and morphological properties of bismuth ferrite nanoparticles. *Ceram. Int.* **2021**, *47*, 3680−3691.

(21) Zhou, M.; Li, W.; Du, Y.; Kong, D.; Wang, Z.; Meng, Y.; Sun, X.; Yan, T.; Kong, D.; You, J. Hydrothermal synthesis of bismuth ferrite Fenton-like catalysts and their properties. *J. Nanoparticle Res.* **2016**, *18*, 1−15.

(22) Basith, M. A.; Yesmin, N.; Hossain, R. Low temperature synthesis of $BiFeO_3$ nanoparticles with enhanced magnetization and promising photocatalytic performance in dye degradation and hydrogen evolution. *RSC Adv.* **2018**, *8*, 29613−29627.

(23) Vishwakarma, A. K.; Tripathi, P.; Srivastava, A.; Sinha, A. S. K.; Srivastava, O. N. Band gap engineering of Gd and Co doped $BiFeO_3$ and their application in hydrogen production through photoelectrochemical route. *Int. J. Hydrogen Energy* **2017**, *42*, 22677−22686.

(24) Betancourt-Cantera, L. G.; Bolarín-Miró, A. M.; Cortés-Escobedo, C. A.; Hernández-Cruz, L. E.; Sánchez-De Jesús, F. Structural transitions and multiferroic properties of high Ni-doped $BiFeO_3$. *J. Magn. Magn. Mater.* **2018**, *456*, 381−389.
(25) Tan, G. Q.; Zheng, Y. Q.; Miao, H. Y.; Xia, A.; Ren, H. J. Controllable microwave hydrothermal synthesis of bismuth ferrites and photocatalytic characterization. *J. Am. Ceram. Soc.* **2012**, *95*, 280−289.
(26) Ren, L.; Lu, S. Y.; Fang, J. Z.; Wu, Y.; Chen, D. Z.; Huang, L. Y.; Chen, Y. F.; Cheng, C.; Liang, Y.; Fang, Z. Q. Enhanced degradation of organic pollutants using $Bi_{25}FeO_{40}$ microcrystals as an efficient reusable heterogeneous photo-Fenton like catalyst. *Catal. Today* **2017**, *281*, 656−661.
(27) Wang, G.; Cheng, D.; He, T.; Hu, Y.; Deng, Q.; Mao, Y.; Wang, S. Enhanced visible-light responsive photocatalytic activity of $Bi_{25}FeO_{40}/Bi_2Fe_4O_9$ composites and mechanism investigation. *J. Mater. Sci.: Mater. Electron.* **2019**, *30*, 10923−10933.
(28) Liu, Y.; Guo, H.; Zhang, Y.; Tang, W.; Cheng, X.; Li, W. Heterogeneous activation of peroxymonosulfate by sillenite $Bi_{25}FeO_{40}$: Singlet oxygen generation and degradation for aquatic levofloxacin. *Chem. Eng. J.* **2018**, *343*, 128−137.
(29) Peng, J.; Hojamberdiev, M.; Xu, Y.; Cao, B.; Wang, J.; Wu, H. Hydrothermal synthesis and magnetic properties of gadolinium-doped $CoFe_2O_4$ nanoparticles. *J. Magn. Magn. Mater.* **2011**, *323*, 133−137.
(30) Matin, M. A.; Hossain, M. N.; Hakim, M. A.; Islam, M. F. Effects of Gd and Cr co-doping on structural and magnetic properties of $BiFeO_3$ nanoparticles. *Mater. Res. Express* **2019**, *6*, 055038.
(31) Nadeem, M.; Khan, W.; Khan, S.; Husain, S.; Singh, F.; Ansari, A.; Shukla, D. K.; Ahad, A.; Chakradhary, V. K.; Akhtar, M. J. Structural, optical and enhanced multiferroic properties of La/Cr co-substituted $BiFeO_3$ nanostructures. *J. Mater. Sci.: Mater. Electron.* **2020**, *31*, 11177−11194.
(32) Gu, Y.; Zhao, J.; Zhang, W.; Zheng, H.; Liu, L.; Chen, W. Structural transformation and multiferroic properties of Sm and Ti co-doped $BiFeO_3$ ceramics with Fe vacancies. *Ceram. Int.* **2017**, *43*, 14666−14671.
(33) Li, W.; Zhang, Y.; Liu, Y.; Cheng, X.; Tang, W.; Zhao, C.; Guo, H. Kinetic performance of peroxymonosulfate activated by Co/$Bi_{25}FeO_{40}$: radical and non-radical mechanism. *J. Taiwan Inst. Chem. Eng.* **2019**, *100*, 56−64.
(34) Maleki, H.; Zakeri, M.; Fathi, R. Experimental study of the effect of yttrium on the structural, thermal, and magnetic properties of $BiFeO_3$. *Appl. Phys. A* **2018**, *124*, 728.
(35) Deng, C.; Wei, X.; Liu, R.; Du, Y.; Pan, L.; Zhong, X.; Song, J. Synthesis of sillenite-type $Bi_{36}Fe_2O_{57}$ and elemental bismuth with visible-light photocatalytic activity for water treatment. *Front. Mater. Sci.* **2018**, *12*, 415−425.
(36) Kang, J. G.; Min, B. K.; Sohn, Y. Synthesis and characterization of $Gd(OH)_3$ and Gd_2O_3 nanorods. *Ceram. Int.* **2015**, *41*, 1243−1248.
(37) Mullica, D. F.; Lok, C. K. C.; Perkins, H. O.; Benesh, G. A.; Young, V. The X-ray photoemission spectra of $Nd(OH)_3$, $Sm(OH)_3$, $Eu(OH)_3$ and $Gd(OH)_3$. *J. Electron Spectrosc. Relat. Phenom.* **1995**, *71*, 1−20.
(38) Sarkar, B.; Dalal, B.; De, S. K. Large exchange bias effect in $LaCr_{0.9}Ru_{0.1}O_3$. *J. Magn. Magn. Mater.* **2016**, *417*, 160−164.
(39) Nechitailov, A. A.; Krasinkova, M. V.; Mokrushina, E. V.; Petrov, A. A.; Kartenko, N. F.; Prokofiev, V. V. Correlation between the impurity content, the average charge state of chromium cations and optical absorption in sillenite crystals doped by chromium in wide range of concentrations. *Cryst. Res. Technol.: J. Exp. Ind. Crystallogr.* **2001**, *36*, 147−156.
(40) Jain, S.; Shah, J.; Negi, N. S.; Sharma, C.; Kotnala, R. K. Significance of interface barrier at electrode of hematite hydroelectric cell for generating ecopower by water splitting. *Int. J. Energy Res.* **2019**, *43*, 4743−4755.
(41) Tan, H.; Zhao, Z.; Zhu, W. B.; Coker, E. N.; Li, B.; Zheng, M.; Yu, W.; Fan, H.; Sun, Z. Oxygen Vacancy Enhanced Photocatalytic Activity of Pervoskite $SrTiO_3$. *ACS Appl. Mater. Interfaces* **2014**, *6*, 19184−19190.
(42) He, C.; Gu, M. Photocatalytic activity of bismuth germanate $Bi_{12}GeO_{20}$ powders. *Scr. Mater.* **2006**, *54*, 1221−1225.
(43) Lin, X.; Huang, F.; Wang, W.; Xia, Y.; Wang, Y.; Liu, M.; Shi, J. Photocatalytic activity of a sillenite-type material $Bi_{25}GaO_{39}$. *Catal. Commun.* **2008**, *9*, 572−576.
(44) Skorikov, V. M.; Zakharov, I. S.; Volkov, V. V.; Spirin, E. A. Steady-state photocurrent characteristics in sillenite crystals. *Inorg. Mater.* **2002**, *38*, 245−251.
(45) Bibi, N.; Sayed, M.; Shah, N. S.; Rehman, F.; Naeem, A.; Mahmood, T.; Hussain, S.; Iqbal, J.; Gul, I.; Gul, S.; Bushra, M. Development of zerovalent iron and titania (Fe^0/TiO_2) composite for oxidative degradation of dichlorophene in aqueous solution: synergistic role of peroxymonosulfate (HSO_5^-). *Environ. Sci. Pollut. Res.* **2022**, 1−16.
(46) Ahmad, S.; Sultan, A.; Raza, W.; Muneer, M.; Mohammad, F. Boron nitride based polyaniline nanocomposite: Preparation, property, and application. *J. Appl. Polym. Sci.* **2016**, *133*, 43989.
(47) Kiashemshaki, H.; Mahvi, A. H.; Najafpoor, A. A.; Hosseinzadeh, A. Investigation of the Efficiency of the Conventional Water Treatment Processes Employed to Eliminate TOC in Jalaliyeh Water Treatment Plant, Tehran. *Health Scope* **2017**, *6*, No. e61907.
(48) Das, S.; Dutta, S.; Tama, A. M.; Basith, M. A. Nanostructured $LaFeO_3$-MoS_2 for efficient photodegradation and photocatalytic hydrogen evolution. *Mater. Sci. Eng. B* **2021**, *271*, 115295.
(49) Barbero, N.; Vione, D. Why Dyes Should Not Be Used to Test the Photocatalytic Activity of Semiconductor Oxides. *Environ. Sci. Technol.* **2016**, *50*, 2130−2131.
(50) Jianmin, L.; Song, J.; Chen, J.; Yu, S.; Jin, D.; Cheng, J. PVA (Polyvincyl Acohol)-assisted hydrothermal preparation of $Bi_{25}FeO_{40}$ and its Photocatalytic Activity. *Mater. Res. Soc. Symp. Proc.* **2009**, *1217*, 322.
(51) Vavilapalli, D. S.; Melvin, A. A.; Bellarmine, F.; Mannam, R.; Velaga, S.; Poswal, H. K.; Dixit, A.; Ramachandra Rao, R.; Singh, S. Growth of sillenite $Bi_{12}FeO_{20}$ single crystals: structural, thermal, optical, photocatalytic features and first principle calculations. *Sci. Rep.* **2020**, *10*, 22052.
(52) Verma, M. K.; Kumar, A.; Singh, L.; Sonwani, R. K.; Das, T.; Singh, S.; Kumar, V.; Singh, N. B.; Mandal, K. $Bi_{25}FeO_{40}$ polycrystalline ceramic as highly efficient photocatalyst synthesised via economical chemical route. *Mater. Technol.* **2020**, *35*, 483−493.
(53) Guo, R.; Fang, L.; Dong, W.; Zheng, F.; Shen, M. Enhanced Photocatalytic Activity and Ferromagnetism in Gd Doped $BiFeO_3$ Nanoparticles. *J. Phys. Chem. C* **2010**, *114*, 21390−21396.
(54) Nethercot, A. H., Jr Prediction of Fermi energies and photoelectric thresholds based on electronegativity concepts. *Phys. Rev. Lett.* **1974**, *33*, 1088.
(55) Huang, Y.; Zhang, X.; Zhu, G.; Gao, Y.; Cheng, Q.; Cheng, X. Synthesis of silver phosphate/sillenite bismuth ferrite/graphene oxide nanocomposite and its enhanced visible light photocatalytic mechanism. *Sep. Purif. Technol.* **2019**, *215*, 490−499.
(56) Banoth, P.; Sohan, A.; Kandula, C.; Kanaka, R. K.; Kollu, P. Microwave-Assisted Solvothermal Route for One-Step Synthesis of Pure Phase Bismuth Ferrite Microflowers with Improved Magnetic and Dielectric Properties. *ACS Omega* **2022**, *7*, 12910−12921.
(57) Mao, W.; Wang, X.; Chu, L.; Zhu, Y.; Wang, Q.; Zhang, J.; Yang, J.; Li, X. A.; Huang, W. Simultaneous enhancement of magnetic and ferroelectric properties in Dy and Cr co-doped $BiFeO_3$ nanoparticles. *Phys. Chem. Chem. Phys.* **2016**, *18*, 6399−6405.
(58) Sharmin, F.; Chandra Roy, D. C.; Basith, M. A. Photocatalytic water splitting ability of Fe/MgO-rGO nanocomposites towards hydrogen evolution. *Int. J. Hydrogen Energy* **2021**, *46*, 38232−38246.

https://doi.org/10.1021/acsomega.2c03457
ACS Omega 2022, 7, 34901−34911